Construction and Building Materials 394 (2023) 132264

Contents lists available at ScienceDirect

Construction and Building Materials

journal homepage: www.elsevier.com/locate/conbuildmat

Performance of reinforced lightweight geopolymer composite panels subjected to windborne debris impacts

Zhixing Li [a], Wensu Chen [a,*], Hong Hao [b,a,*]

[a] Centre for Infrastructural Monitoring and Protection, School of Civil and Mechanical Engineering, Curtin University, Australia
[b] Earthquake Engineering Research & Test Center, Guangzhou University, China

ARTICLE INFO

Keywords:
Lightweight geopolymer composite (LGC) panel
Windborne debris impact
Impact resistance capacity
Pneumatic cannon testing

ABSTRACT

Lightweight panels have been widely employed as building envelopes in construction. As a result of the rising demand for environmentally friendly building materials, the authors recently developed a lightweight geopolymer composite (LGC) material and investigated the performance of reinforced LGC panels under static loading. Superior performance of LGC panels as compared to conventional panels such as autoclaved aerated concrete (AAC) panels has been observed, demonstrating their potential applications. During strong winds, building envelopes might be subjected to windborne debris impact, which could threaten residents and facilities and lead to structural failure. To explore the application potentials of LGC panels in strong wind regions, in this study, the performances of LGC panels subjected to windborne debris impact were investigated and compared with those of AAC panels by using a pneumatic cannon testing system. The failure modes and damage levels under different impact scenarios of LGC and AAC panels and their impact resistance capacities were obtained, compared and quantified in terms of the projectile residual velocity, penetration length and opening size. The effects of matrix materials, panel thicknesses, impact locations, reinforcement spacings and projectile impact velocities on their impact resistance performance were analyzed. For comparison, the punching shear capacities of the panels were also quasi-statically tested and analyzed subjected to the same projectile employed in the impact tests.

1. Introduction

Prefabricated construction technology is considered as a sustainable construction method due to its affordability, energy efficiency and sustainability [1,2]. Reinforced autoclaved aerated concrete (AAC) panels have been widely used as prefabricated lightweight building envelopes (e.g., external cladding walls, roofs and floors) in domestic and industrial constructions, as shown in Fig. 1. There is a growing demand for sustainable construction by using lightweight sustainable materials with high strength-to-weight ratios, good thermal insulation, sound absorption and fire resistance [3,4]. A new lightweight geopolymer composite (LGC) material has been developed by the authors [5,6], and the responses of reinforced lightweight panels made of this newly developed LGC under static loadings were studied for application to prefabricated structures [7]. The results showed that the LGC panels have better structural performance in terms of load-carrying capacity as compared to AAC panels, and can meet the requirement for the applications to prefabricated building envelopes (i.e., cladding walls, roofs and floors) [8].

In recent years, the intensity and occurrence of strong wind events have increased due to climate change. According to post-storm investigations, an immense amount of windborne debris was generated, which has been the major cause of damage to building envelopes during strong wind events [11]. The perforation of windborne debris can impose severe risks to residents and facilities inside the building, even resulting in structural failure [12], as shown in Fig. 2. A dominant opening could be created due to windborne debris penetrating through the building envelopes. As a result, the increased loads on the building envelope (i.e., roofs and walls) due to internal pressurization might result in roof lift-up or wall collapse. Therefore, the structural integrity and the penetration resistance capacity of the reinforced lightweight panel are essential for the safety of the residents and structures when it is used as building envelope in strong wind regions [13]. In Australia, the windborne debris impact needs to be considered in structural design, that is, the penetration resistance capacity of the building envelope to withstand windborne debris should satisfy the requirements as per the

* Corresponding authors.
E-mail addresses: wensu.chen@curtin.edu.au (W. Chen), hong.hao@curtin.edu.au (H. Hao).

https://doi.org/10.1016/j.conbuildmat.2023.132264
Received 18 October 2022; Received in revised form 20 June 2023; Accepted 21 June 2023
Available online 28 June 2023

design codes such as AS/NZS 1170.2:2021 [14].

In recent decades, the response of reinforced concrete (RC) slabs/panels subjected to localized impact has been intensively investigated. It is reported that the response and damage modes of slabs/panels are significantly affected by concrete strength and reinforcement configuration [17]. Several experimental studies were conducted to evaluate the effect of concrete strength on the impact resistance of RC slabs [18–22]. The high strength of concrete can significantly enhance the capacity of RC slabs/panels to resist penetration. The effect of reinforcement in the RC panels on the penetration resistance capacity was also investigated [23–26]. In addition, factors such as reinforcement ratios, materials of reinforcement and locations of the reinforcement affect its impact resistance capacity and failure modes. For example, Sadraie et al. [26] reported that the performance of slabs is enhanced by increasing the reinforcement ratio or the slab thickness under drop weight impact loads. The size and spacing of reinforcement mesh also affect the impact resistance of concrete panels. Abbas et al. [27] investigated the effect of reinforcement spacing on quasi-static and dynamic punching loads. The 600 mm × 600 mm × 90 mm panels reinforced by two steel-mesh spacings of 25 and 100 mm with the same reinforcement ratio were tested. It illustrated that closely spaced rebars with smaller diameters were more effective in reducing damage levels and enhancing perforation resistance. Therefore, to improve the perforation resistance, the mesh spacing of reinforcement was recommended to be less than the nominal cross-section of the projectile to ensure the impact on the steel mesh [25].

Most previous studies focused on the performance of reinforced panels under impact loads with high velocity in the range of 100–300 m/s. However, limited studies on the performance of reinforced concrete panels subjected to windborne debris impact (with the velocity under 50 m/s) have been reported in the literature. Nevins [28] experimentally studied the penetration resistance capacity of RC slabs with the thickness of 152.4–254.0 mm against a 6.8 kg wooden projectile at the impact velocity range of 15.6–33.0 m/s. Carter [29] reported that windborne debris with the velocity of 16.1–34.9 m/s results in extensive radial cracks and scabbing at the distal face of RC walls with different thicknesses. Kulkarni and Shafei [30] studied the performance of concrete wall panels subjected to projectile impact in the range of 10–70 m/s and reported that steel rebars enhanced the performance of reinforced wall panels under windborne debris impact. In addition, the performances of building envelopes, such as structural insulated panels and corrugated panels, subjected to windborne debris impact have been symmetrically investigated by authors [31–38]. However, no study on the thin reinforced lightweight panels subjected to windborne debris impact can be found in the literature yet. Hence, it is essential to investigate the performance of reinforced lightweight panels subjected to windborne debris impact.

This study experimentally investigated the performance of AAC and LGC panels subjected to windborne debris impact by using a pneumatic cannon testing system. Six AAC panels and 20 LGC panels with different configurations were tested under a 4 kg wooden projectile impact with velocities in the range of 18–28 m/s as per AS/NZS 1170.2:2021 [14]. The dynamic responses were examined quantitatively in terms of projectile residual velocity, penetration length and opening size. The effects of matrix materials, impact velocities, impact locations, panel thicknesses and reinforcement spacings on their performance were examined. The specimens with different configurations were also quasi-statically tested under punching shear loads using the same wooden projectile employed in the impact tests. The failure modes were observed and compared with those under projectile impact.

2. Experimental program

Windborne debris impact tests were conducted as per AS/NZS 1170.2:2021 [14]. As specified, the structural component should be able to withstand the impact of windborne debris, which is represented by a 4 kg wooden projectile with a nominal cross-section of 100 mm × 50 mm. The impacting velocity of the projectile is specified as 0.4 V_R for horizontal trajectory and 0.1 V_R for vertical trajectory, respectively, in which V_R is the regional wind speed. The structural panel used as building envelope is classified as Importance Level 2 with the specified annual probability exceedance of 500 years for wind as per the Building Code of Australia (NCC 2022) [39]. For instance, the specified design V_R values are 45, 57 and 69 m/s at regions A, B and C, respectively, which correspond to the projectile impact velocities of 18, 23 and 27 m/s, respectively. For comparison, the specimens were also tested under quasi-static punching shear loads using the wooden projectile, which was used for the impact test.

2.1. Design and manufacturing of specimen

In this study, the commercially used AAC panels in construction were provided by a local supplier named Westgyp [9]. The LGC panels were fabricated by using the mix design of ambient-cured LGC with 30% EPS in volume developed in the previous study [5], as presented in Table 1. Low calcium fly ash and slag, silica sand and EPS beads were used as binder materials, fine aggregates and lightweight aggregates, respectively. The mixed solution of D-grade sodium silicate (Na_2SiO_3) and 8 M (molarity = 8 mol/L) sodium hydroxide (NaOH) solution was used as alkaline activator. The mass ratios of fly ash to slag and alkaline activator to binder were determined as 5.6 and 0.4, respectively. The manufacturing process of LGC panels is detailed in Fig. 3 [5]. At least three sulphur-capped cylindrical specimens (Ø100 mm × 200 mm) for each configuration were tested to determine the material compressive strength by using MATEST testing machine with the loading rate of 0.33 MPa/min as per ASTM C39-18 [40]. The material properties of AAC and LGC are summarised in Table 2 [7].

Four specimens (i.e., one panel for each configuration) (Fig. 4.) were prepared for the quasi-static punching shear test, and 26 specimens, including 6 AAC panels and 20 LGC panels, were prepared for the impact

Fig. 1. Prefabricated AAC panel construction: (a) schematic illustration [9] and (b) photograph [10].

test. All the panels used in this study had the same dimension of 640 mm × 600 mm. The commercially available AAC panel with the thickness of 50 mm (namely AAC_T50L) was reinforced by one layer of Ø 3.2 mm welded steel mesh in the transverse and longitudinal directions. The effective depth of the steel mesh was 25 mm. LGC_T37L with a thickness of 37.5 mm, having a similar weight as AAC_T50L of thickness 50 mm, was prepared to compare the structural performance of AAC and LGC panels with the same weight. To investigate the effect of using LGC as matrix material, LGC_T50L specimens with the thickness of 50 mm were constructed with the same mesh configuration as AAC_T50L. To study the influence of reinforcement spacing, LGC_T50S had the same dimension as LGC_T50L but was reinforced by using the 2.5 mm-diameter welded steel mesh with smaller mesh grids (i.e., 98 mm × 100 mm), which consisted of six steel wires in the transverse direction and seven steel wires in the longitudinal direction to maintain a constant reinforcement ratio. The specifications of the specimens are given in Table 3.

2.2. Experimental methodology and equipment

2.2.1. Quasi-static punching shear test

Before conducting windborne debris impact tests, the panels were tested under quasi-static punching shear loads. Fig. 5 illustrates the laboratory setup of quasi-static punching shear test, including a load cell, hydraulic jack, linear variable differential transformer (LVDT), data acquisition system and wooden projectile. The loading was applied through a wooden projectile with a nominal cross-section of 100 mm × 50 mm, which was also used as the projectile for the windborne debris impact test. The specimens with the effective dimension of 560 mm × 500 mm at the distal face were clamped at the four edges (same as in the impact test) and subjected to quasi-static punching shear loads with an equivalent loading rate of 1 mm/min until failure. The location of the applied load was at the center of the specimen in such a manner that no steel mesh of AAC_T50L, LGC_T37L and LGC_T50L panels was in the loading area. For LGC_T50S specimens, however, the steel mesh existed in the projectile loading area due to the close spacing of the steel mesh.

2.2.2. Pneumatic cannon impact test

In the impact test, the projectile was launched at the desired velocity by using a pneumatic cannon, which was used to simulate debris driven by the wind. Fig. 6 (a) and Fig. 6 (b) illustrate the schematic diagram and laboratory setup of the pneumatic cannon impact test, respectively, including the pneumatic cannon, steel support frame, high-speed cameras and halogen lights. As shown in Fig. 7, the specimens were clamped peripherally onto the support frame, which had the effective dimension of 560 mm × 500 mm at the distal face and was located 4 m away from the pneumatic cannon. The pneumatic cannon included a 3 m barrel, a chamber and an air compressor. A 4 kg wooden rod with cross-sectional dimensions of 100 mm × 50 mm was used as projectile as per AS/NZS 1170.2:2021 [14]. Two high-speed cameras were used to capture the projectile striking and residual velocity, as well as the damage process of the specimens from the proximal and distal faces. The projectile impacted onto the specimens at various locations of the panel including plain matrix (PM), steel wire (SW) and wire intersection (WI), as illustrated in Fig. 8.

Table 1
Mix proportion of LGC [5].

Constituent	Fly ash	Slag	NaOH	Na_2SiO_3	Sand	EPS
Weight (kg/m^3)	595	105	80	200	325	4

3. Experimental results

3.1. Quasi-static punching shear test

Fig. 9 (a)–9 (d) show the failure pattern of reinforced lightweight panels subjected to quasi-static punching shear loads. The steel wires around the location of the applied load are indicated in black dashed lines. AAC_T50L failed in punching shear patterns, and a typical shear plug was formed, with indentation observed at the proximal face and only punching shear cracks formed at the distal face. The AAC material as a porous and brittle material has a fraction volume of pores around 65%–90% and an extremely low modulus of rupture of 0.5 MPa. Therefore, the shear plug was formed when the shear strength was reached along the plug surface. Compared with AAC panels, LGC panels primarily failed in flexural modes, that is, flexural yield lines extending from the loading location to the panel boundary were observed on the distal face of the specimens due to the relatively higher stiffness and flexibility of the LGC panels, as shown in Fig. 9 (b)–9 (d). It was reported that conventional RC panels with low thickness tended to fail in flexural mode by generating radial yield lines [41]. Therefore, the LGC panels with different configurations obtained comparable flexural behavior to the conventional RC panels under punching shear loads. The closer spacing of steel mesh in LGC_T50S specimens did not change the cracking pattern as compared to LGC_T50L. This observation was consistent with a previous study on the effect of rebar spacing on the behavior of RC panels under quasi-static punching shear loads [27]. Additionally, the LGC specimen with the thickness of 37.5 mm experienced more severe damage than the 50 mm-thickness LGC specimens. The indentation and extensive cracks were observed on the proximal face of the LGC_T37L specimen.

The load–deflection curves of all tested panels are presented in Fig. 10. The central deflection was recorded by an LVDT located at the midspan of the slab. All specimens behaved linearly up to the cracking load, beyond which the behavior was nonlinear until failure. A slight fall in the load–deflection curve was observed after reaching the first crack

(a) (b)

Fig. 2. Windborne debris impact: (a) Hurricane Harvey (2017) in Texas Coast [15], and (b) Tornado Alley (1999) in Oklahoma and Kansas [16].

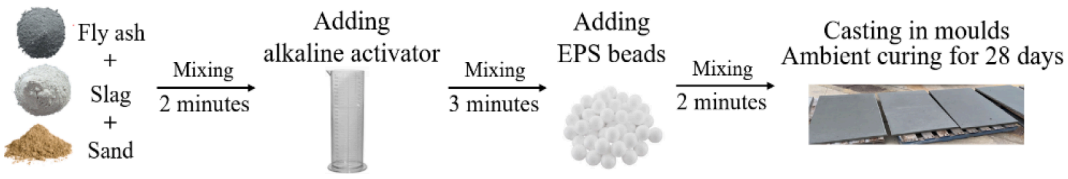

Fig. 3. Manufacturing process of LGC panels.

Table 2
Material properties of AAC and LGC [7].

Material	ρ (SD) (kg/m^3)	f_c'(SD) (MPa)	f_r (SD) (MPa)	E (SD) (GPa)
AAC	765 (20.08)	4.18 (0.33)	0.50 (0.08)	1.18 (0.10)
LGC	1033 (28.5)	12.75 (1.4)	1.02 (0.12)	4.83 (0.03)

Note: ρ = density; f_c' = compressive strength of cubic specimen; f_r = modulus of rupture; E = modulus of elasticity; and SD = standard deviation.

load. The LGC specimens exhibited higher initial stiffness than the AAC panel, which led to a higher cracking load of the LGC panels at the cracking point, resulting from the higher strength of LGC material. For instance, the cracking loads of LGC_T37L, LGC_T50L and LGC_T50S were 1.2 kN, 4.2 kN and 3.6 kN, respectively, which were much higher than that of AAC_T50L (i.e., 0.4 kN). As shown in Fig. 10, the deflection of LGC_T50L at the cracking load was 3 mm, which was higher than those of other configurations (i.e., around 1.75 mm). For the AAC_T50L panel,

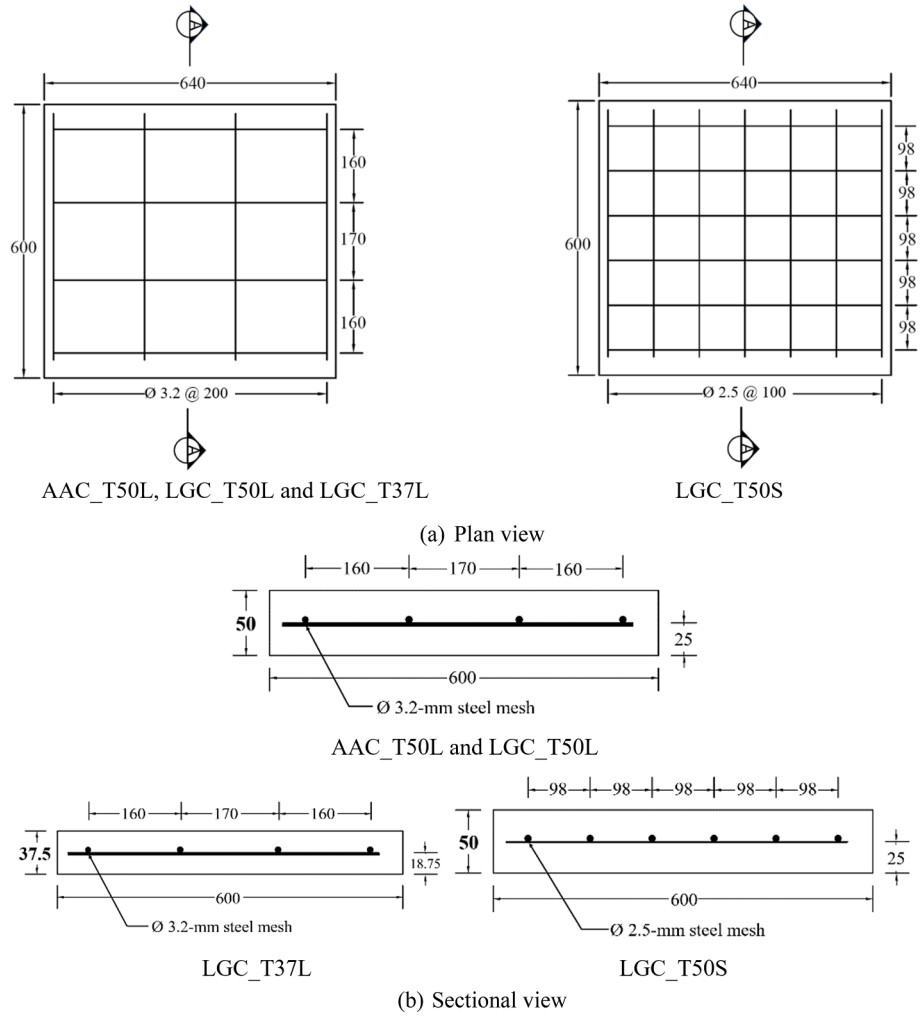

Fig. 4. Schematic diagram of the panels (unit: mm): (a) plan view and (b) sectional view.

Table 3
Description of testing specimens.

ID	Material	Compressive strength (MPa)	Weight (kg)	Length × Width (mm)	Thickness (mm)	Diameter of steel mesh (mm)	Reinforcement ratio (%)
AAC_T50L	AAC	2.8	13	640 × 600	50.0	3.2	0.11
LGC_T37L	LGC	7.2	13	640 × 600	37.5	3.2	0.14
LGC_T50L	LGC	7.8	20	640 × 600	50.0	3.2	0.11
LGC_T50S	LGC	7.6	20	640 × 600	50.0	2.5	0.11

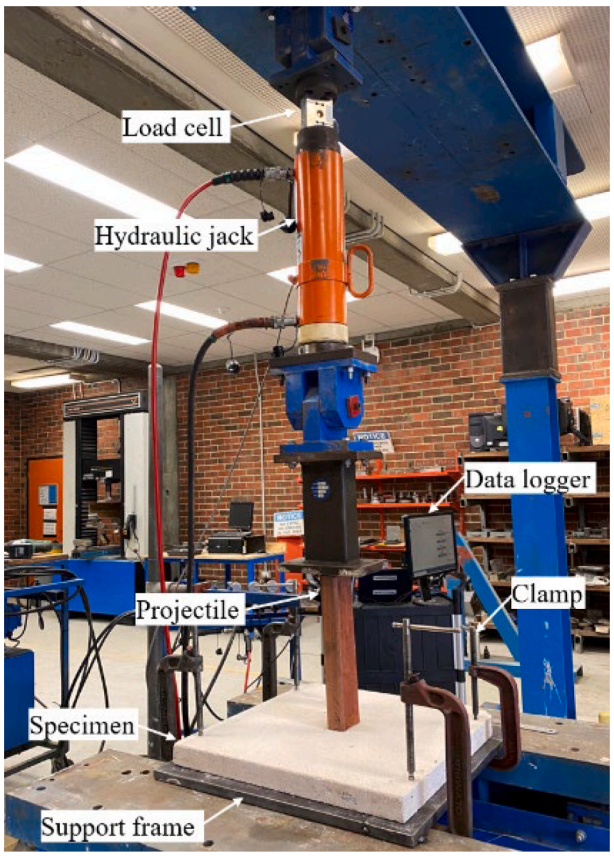

Fig. 5. Quasi-static punching shear test setup.

this difference can be attributed to the lower strength and toughness of the AAC matrix. For the LGC_T37L panel, the reduced thickness is the primary contributing factor. For the LGC_T50S panel, the densely spaced mesh can lead to stress concentration, particularly around the regions where the mesh is located, causing concrete to crack more easily in those areas as compared to LGC_T50L with similar reinforcement ratio and concrete strength. The decreased cracking strength with densely spaced mesh was also reported in the previous study [42] on the effect of mesh spacing on the performance of slab. In addition, the LGC_T50S and LGC_T50L specimens obtained similar ultimate loading capacities of 7.0 and 6.5 kN, respectively, followed by LGC_T37L (i.e., 4.4 kN) and AAC_T50L (i.e., 3.0 kN). The experimental results demonstrated that LGC panels have better load-carrying capacity than AAC panels.

LGC is made of by-products or waste material such as fly ash, slag and EPS. Utilizing LGC as matrix material can promote more sustainable practices in the construction industry, both in terms of embodied energy and greenhouse gas emissions, when compared to OPC-based products [43,44]. Although the production process of alkali-activators, including sodium silicate and sodium hydroxide, contributes to energy consumption and greenhouse gas emissions, the overall environmental benefits of using geopolymer outweigh the drawback as the amount of alkali-activators used in geopolymer constitutes only a minor portion of its total weight. For instance, each ton of OPC-based material requires 3.2–6.3 GJ of energy [45,46]. As for the raw material of geopolymer, it was reported that the energies required to produce one metric ton of FA, slag and sand were approximately 0.033, 0.857 and 0.081 GJ/t, respectively [47–49]. Moreover, the production of sodium hydroxide solution (8 M) and sodium silicate solution required 5.125 and 5.371 GJ/t, respectively [50,51]. Therefore, the embodied energy required to produce LGC in this study is calculated as 1.236 GJ/t, which is substantially lower than that of OPC-based materials. Furthermore, the production of one kilogram of processed OPC typically generated around 0.85 to 0.92 kg of CO_2 emissions [52,53], whereas one kilogram

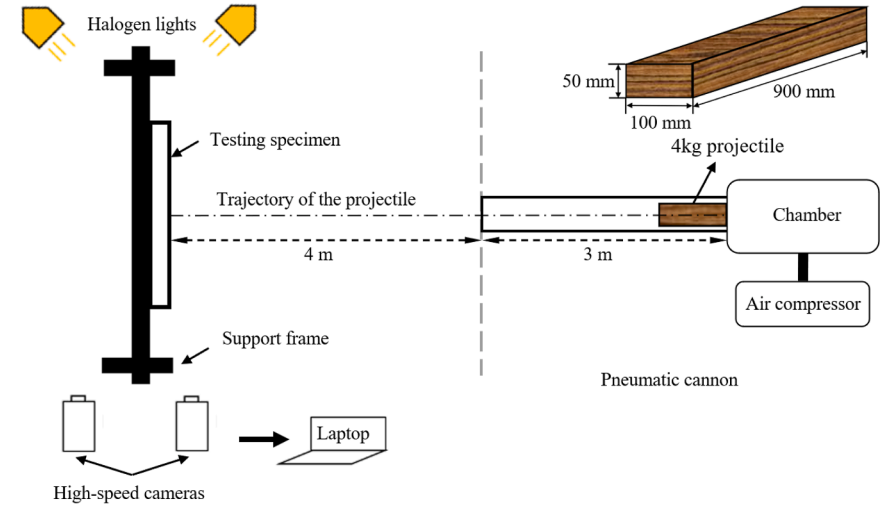

(a)

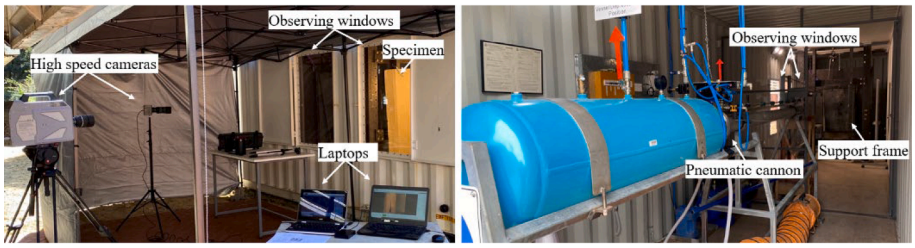

(b)

Fig. 6. Pneumatic cannon impact test setup: (a) schematic diagram and (b) photograph.

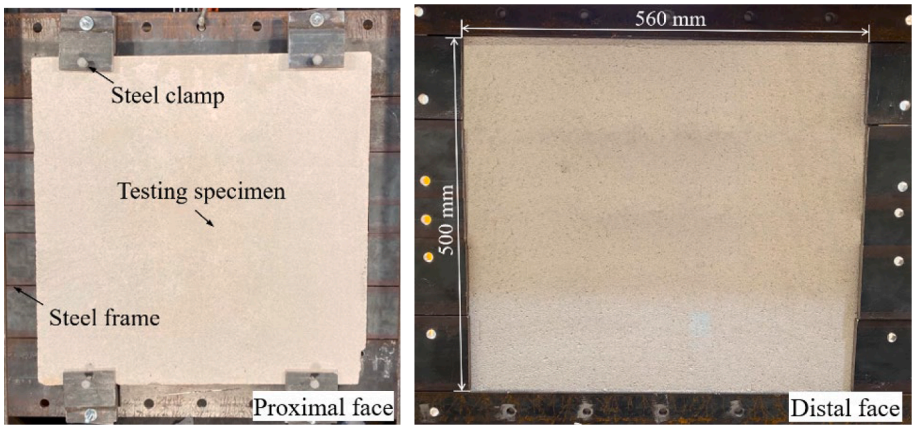

Fig. 7. Photograph of testing panel.

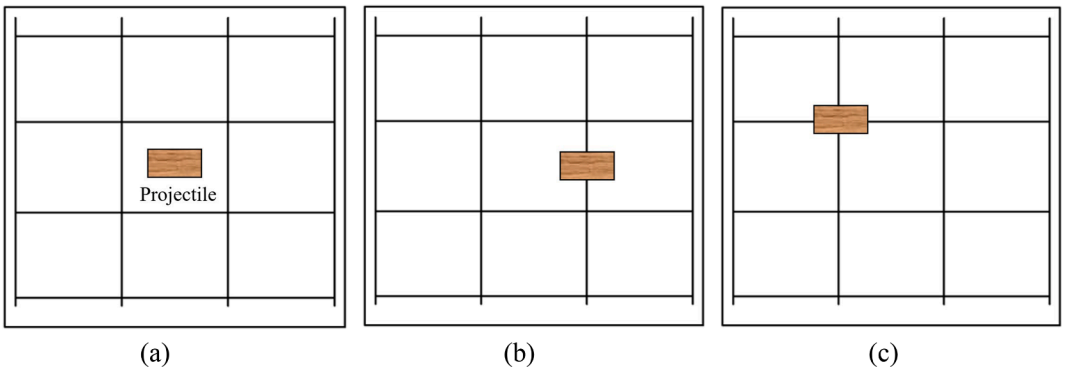

Fig. 8. Schematic diagram of impact location: (a) plain matrix (PM), (b) steel wire (SW) and (c) wire intersection (WI).

of ambient-cured LGC resulted in average equivalent CO_2 emissions of around 0.3 kg [54]. Therefore, the adoption of LGC panels in construction not only enhances the load-carrying capacity of the panel, but also reduces greenhouse gas emissions in construction, contributing to achieving the carbon–neutral goal for environment protection.

3.2. Pneumatic cannon impact test

The performance of reinforced lightweight panels against windborne debris impact was investigated, and the effects of matrix materials, panel thicknesses, reinforcement spacings and projectile velocities on the impact resistance performance were studied. The dynamic response of the specimens was studied and recorded in terms of the residual velocity, penetration length (PL), damage level and failure pattern of steel mesh. Various damage levels indicate the amounts of dissipated energy during the impact [55]. According to the test results, three types of failure modes were identified. The projectile penetrating through the specimen was classified as 'penetration and through (PT)'. The projectile penetrating but staying in the specimen was categorized as 'penetration and stay (PS)'. The projectile generating the opening but rebounding by the specimen was classified as 'rebounded (R)'. The cone-shaped plug was formed in all specimens by the projectile impact. The scabbing failure occurred as a result of stress wave propagation and shear deformation with diagonal cracks developing towards the distal face. The equivalent opening diameter at the distal face of the specimen was defined as the mean value of opening dimensions measured in different orientations (i.e., horizontal, vertical and two diagonal) by Eq. (1), as shown in Fig. 11 [25,56].

$$D_{eq} = (D_h + D_v + D_{d1} + D_{d2})/4 \quad (1)$$

where D_{eq} denotes the equivalent opening diameter at the distal face; D_h and D_v are the diameters in the horizontal and vertical direction, respectively; and D_{d1} and D_{d2} are the diameters along two diagonal directions. The detailed testing scenario and results for the AAC and LGC panels are given in Tables 4–7.

3.2.1. Failure modes of AAC_T50L

Three AAC_T50L specimens (i.e., AAC_T50L_PMA, AAC_T50L_PMB and AAC_T50L_PMC) were impacted at the location of plain matrix (PM). The projectile penetrated through the specimens by creating the opening at the distal face with D_{eq} of 277, 281 and 317 mm and residual velocity of 6.7, 16.6 and 19.1 m/s, corresponding to the impact velocity of 18.4, 23.2 and 28.6 m/s, respectively, as shown in Table 4. Fig. 12 (a) shows the failure modes of AAC_T50L_PMA. The specimen failed in a direct shear punch mode due to the low shear strength of AAC. Through-thickness cone cracking and plugging are formed, because the shear capacity of the panel around the high-impact stress region is exceeded [17]. Fig. 13 shows that the fragments and hairline cracks were generated in the vicinity of the opening at the distal face from the failure process captured by the high-speed camera. The projectile impact caused minimal panel deflection but created a 100 mm × 50 mm clear opening (with similar dimensions to the cross-section of projectile). Partial kinetic energy of the projectile was absorbed by the shear failure of AAC and the friction between panel and projectile. However, the projectile directly penetrates through the panel with a relatively large residual velocity, imposing great threats to people and facilities behind the panel. The opening created on the panel also increases the risk of roof lifting and wall collapsing of the building because of the combined external suction and internal pressures owing to wind entering the building from the opening.

If the projectile impacted onto the wire intersection (WI) of steel mesh, all three specimens (i.e., AAC_T50L_WIA, AAC_T50L_WIB and

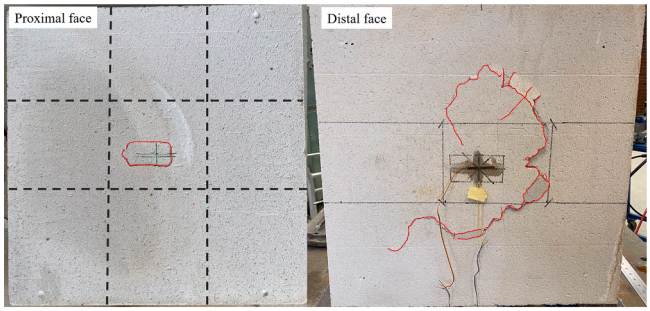

(a) AAC_T50L

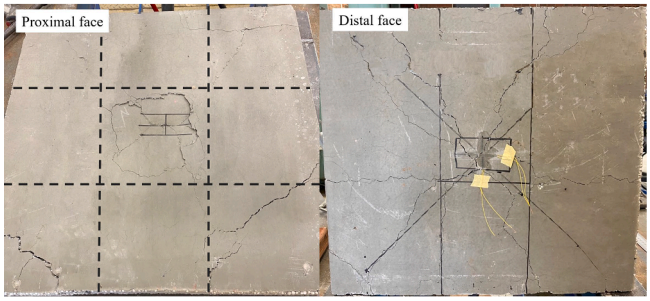

(b) LGC_T37L

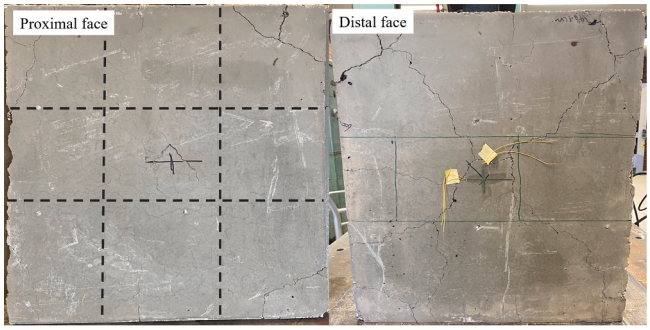

(c) LGC_T50L

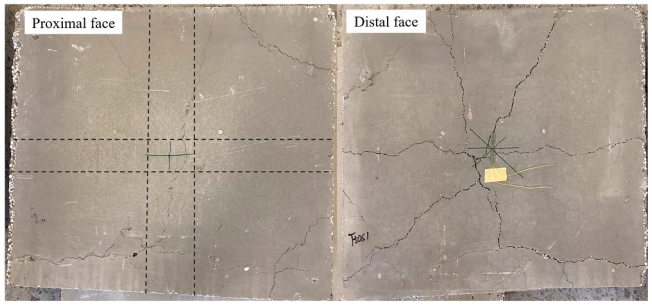

(d) LGC_T50S

Fig. 9. Failure modes of specimens: (a) AAC_T50L, (b) LGC_T37L, (c) LGC_T50L and (d) LGC_T50S.

AAC_T50L_WIC) experienced the global structural response due to the bending of steel mesh, as shown in Fig. 12 (b) and 12 (c). When the impact velocity was 18.2 m/s, the projectile was rejected by the steel mesh with a rebound velocity of −1 m/s but an opening was created, as shown in Fig. 14. The specimen experienced 'penetration and through' with the rupture of the steel mesh when the impact velocities were 23.7 and 28.1 m/s. The opening was created with extensive cracking on the proximal face, which was formed by the punching shear damage and deformation of the steel mesh. At the distal face, the opening was observed and large pieces of AAC fragment were created and held by the steel mesh in the vicinity of the opening, indicating that the failure mode of the specimen was changed to global failure. Shear failure was

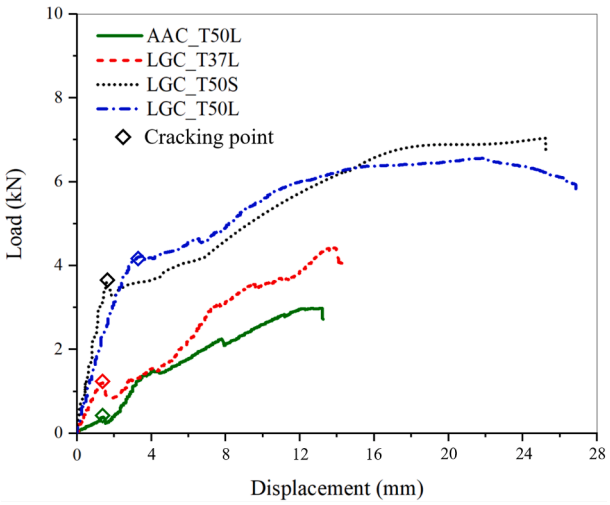

Fig. 10. Load–deflection curves of all the specimens.

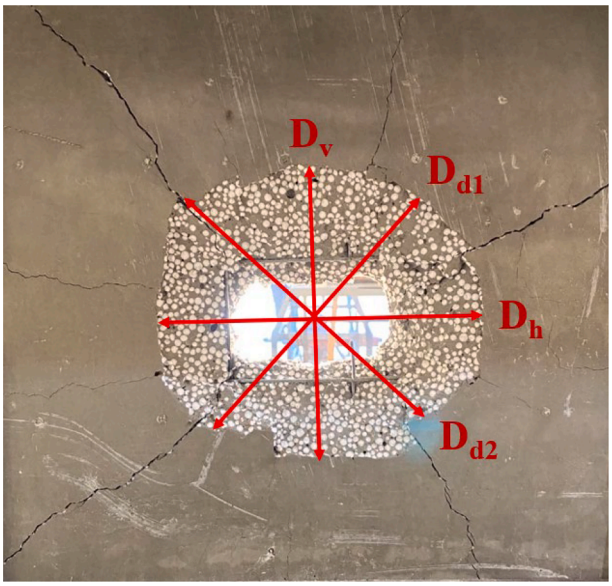

Fig. 11. Equivalent diameter of the opening at the distal face.

initiated in the form of a punching shear plug due to the transient high-shear force. Thereafter, the specimen experienced deflection along with the deformation of steel mesh. The stiffness of the whole specimen was reduced due to the damage of the AAC, and the kinetic energy of the projectile was partially dissipated by the deformation and rupture of steel mesh, and the penetrated projectile still kept large kinetic energy with substantial residual velocity as indicated in Table 4.

3.2.2. *Failure modes of LGC_T37L*

As shown in Table 5, when the impact velocity of the projectile was around 18 m/s, three LGC_T37L specimens (i.e., LGC_T37L_PMA, LGC_T37L_SWA and LGC_T37L_WIA) experienced 'penetration and stay' failure with the penetration lengths of 340, 295 and 90 mm, respectively, corresponding to different impact locations (i.e., PM, SW and WI). For the specimens (i.e., LGC_T37L_PMB, LGC_T37L_SWB and LGC_T37L_WIB) subjected to the impact velocity around 24 m/s, the projectile completely penetrated through the specimen. They experienced similar damage mode to the specimens subjected to the projectile with the impact velocity of 18 m/s. For example, localized punching shear failure was observed in the LGC_T37L_PMA and LGC_T37L_PMB

Table 4
Testing scheme and results of AAC_T50L.

No	Specimen	V_o (m/s)	Impact location	Results	V_r (m/s)	PL (mm)	Damage		
							Opening	Mesh	D_{eq} (mm)
1	AAC_T50L_PMA	18.4	PM	PT	6.7	–	Yes	–	277
2	AAC_T50L_PMB	23.2	PM	PT	16.6	–	Yes	–	281
3	AAC_T50L_PMC	28.6	PM	PT	19.1	–	Yes	–	317
4	AAC_T50L_WIA	18.2	WI	R	−1	–	Yes	Deform	381
5	AAC_T50L_WIB	23.7	WI	PT	11.4	–	Yes	Rupture	407
6	AAC_T50L_WIC	28.1	WI	PT	17.2	–	Yes	Rupture	439

Note: V_o = projectile striking velocity, V_r = projectile residual velocity, PM = plain matrix, WI = wire intersection, PT = penetration and through, R = Rebound, PL = penetration length, "-": not applicable.

Table 5
Testing scheme and results of LGC_T37L.

No	Specimen	V_o (m/s)	Impact location	Results	V_r (m/s)	PL (mm)	Damage		
							Opening	Mesh	D_{eq} (mm)
1	LGC_T37L_PMA	18.5	PM	PS	0	340	Yes	–	202
2	LGC_T37L_PMB	23.9	PM	PT	15.1	–	Yes	–	206
3	LGC_T37L_SWA	18.8	SW	PS	0	295	Yes	Rupture	198
4	LGC_T37L_SWB	24.3	SW	PT	12.6	–	Yes	Rupture	224
5	LGC_T37L_WIA	18.4	WI	PS	0	90	Yes	Deform	239
6	LGC_T37L_WIB	24.1	WI	PT	10.2	–	Yes	Rupture	194

Note: SW = steel wire, PS = penetration and stay.

Table 6
Testing scheme and results of LGC_T50L.

No	Specimen	V_o (m/s)	Impact location	Results	V_r (m/s)	PL (mm)	Damage		
							Opening	Mesh	D_{eq} (mm)
1	LGC_T50L_PMA	18.5	PM	PS	0	243	Yes	–	251
2	LGC_T50L_PMB	23.6	PM	PT	10.28	–	Yes	–	271
3	LGC_T50L_SWA	18.4	SW	R	−0.9	–	Yes	Deform	265
4	LGC_T50L_SWB	23.8	SW	PT	7.95	–	Yes	Rupture	273
5	LGC_T50L_SWC	28.5	SW	PT	14.87	–	Yes	Rupture	297
6	LGC_T50L_WIA	18.8	WI	R	−1	–	Yes	Deform	279
7	LGC_T50L_WIB	24.3	WI	PS	0	129	Yes	Deform	298
8	LGC_T50L_WIC	28.2	WI	PT	11.32	–	Yes	Rupture	312

Table 7
Testing scheme and results of LGC_T50S.

No	Specimen	V_o (m/s)	Impact location	Results	V_r (m/s)	PL (mm)	Damage		
							Opening	Steel mesh	D_{eq} (mm)
1	LGC_T50S_SWA	18.4	SW	PS	0	80	Yes	Rupture	254
2	LGC_T50S_SWB	23.4	SW	PT	7.3	–	Yes	Rupture	279
3	LGC_T50S_SWC	28.6	SW	PT	13.2	–	Yes	Rupture	250
4	LGC_T50S_WIA	18.5	WI	R	−0.8	–	Yes	Deform	266
5	LGC_T50S_WIB	24.5	WI	R	−1.3	–	Yes	Rupture	285
6	LGC_T50S_WIC	27.9	WI	PT	12.8	–	Yes	Rupture	302

specimens with the 100 mm × 50 mm rectangular opening at the proximal face and the enlarged opening at the distal face, as shown in Fig. 15 (a). The specimens provided frictional resistance to the flying projectile, thereby dissipating partial kinetic energy of the projectile. When the projectile impacted onto the steel mesh, the panel demonstrated better performance. As shown in Fig. 15 (b), radial cracks were observed at both the proximal and distal faces of LGC_T37L_SWA and LGC_T37L_WIA, showing punching–flexural failure. The rupture of steel mesh was observed with the impact location at steel wire (SW) and wire intersections (WI) when the impact velocity of the projectile was around 24 m/s, as shown in Fig. 16. Unlike the cases with impact velocity about 18 m/s, the impact kinetic energy was only partially dissipated by the punching shear and flexural damage of the specimen and the deformation of the steel mesh as the penetrated projectile still had a large residual velocity.

3.2.3. *Failure modes of LGC_T50L*

Table 6 summarises the experimental results of LGC_T50L. When the projectile impacted onto the plain matrix (PM) and steel wire (SW), five LGC_T50L specimens experienced similar deformation and damage profiles with different levels, that is, a rectangular opening with similar dimensions to the cross-section of projectile (i.e., 100 mm × 50 mm) at the proximal and an opening with radial cracks at distal face, as shown in Fig. 17 (a) and 17 (b). The extensive radical cracks in the vicinity of the opening were observed at the distal face during the failure process, as shown in Fig. 18. When the impact velocity was around 18 m/s, the projectile penetrated and stayed in the specimen LGC_T50L_PMA with the penetration length of 243 mm, while the projectile was rejected by

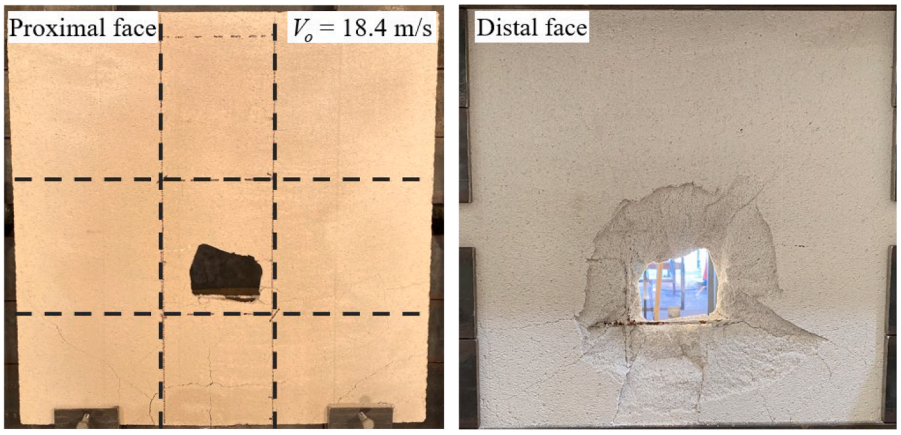

(a) AAC_T50L_PMA

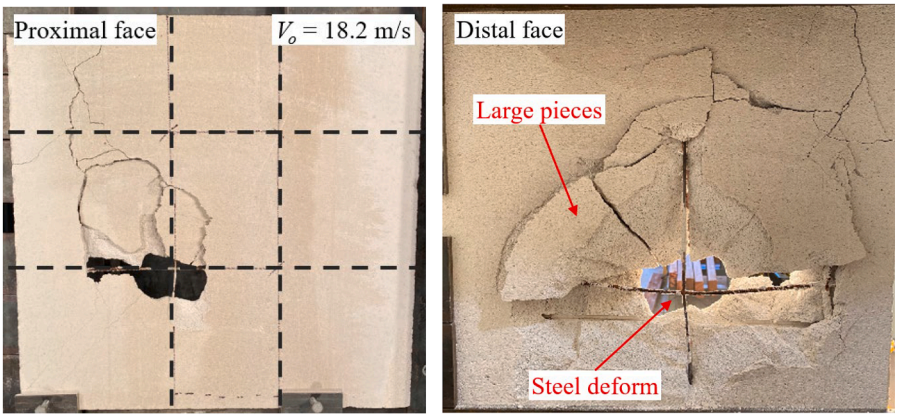

(b) AAC_T50L_WIA

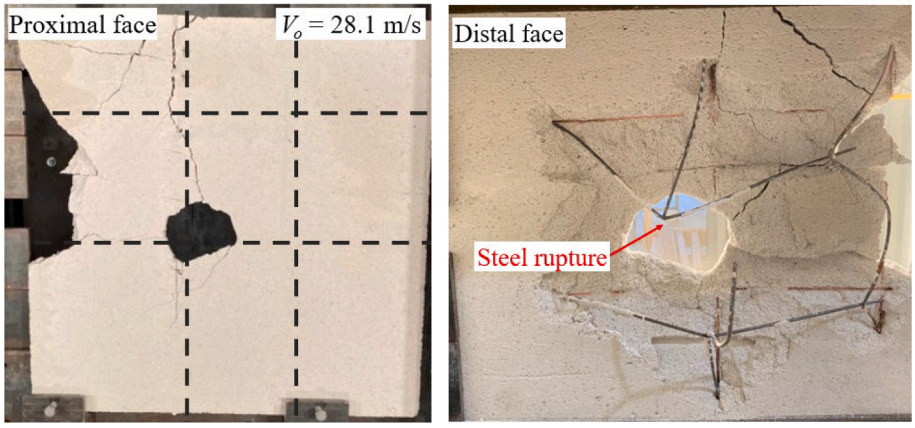

(c) AAC_T50L_WIC

Fig. 12. Photographs of specimens: (a) AAC_T50L_PMA, (b) AAC_T50L_WIA and (c) AAC_T50L_WIC.

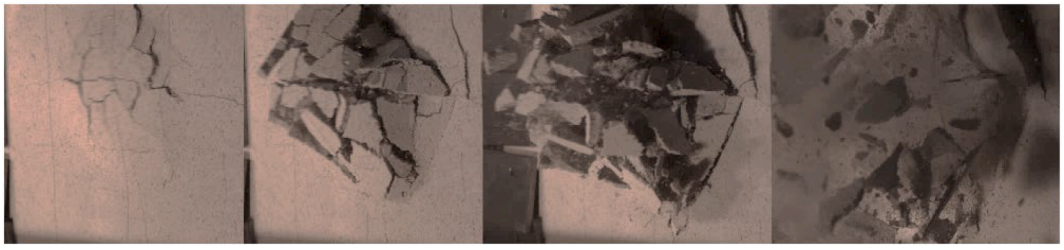

Fig. 13. Typical failure process of AAC_T50L at distal face.

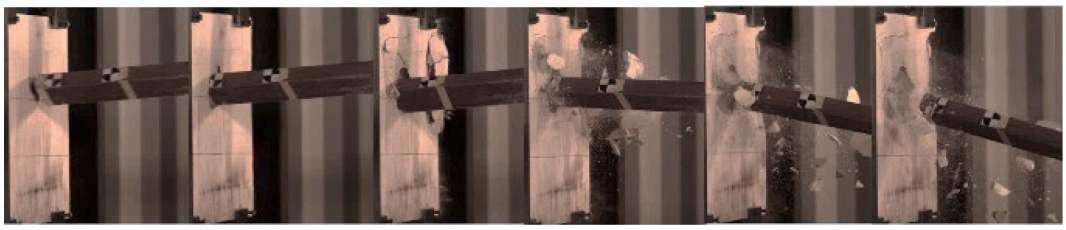

Fig. 14. Rebound of the wooden projectile of specimen AAC_T50L_WIA.

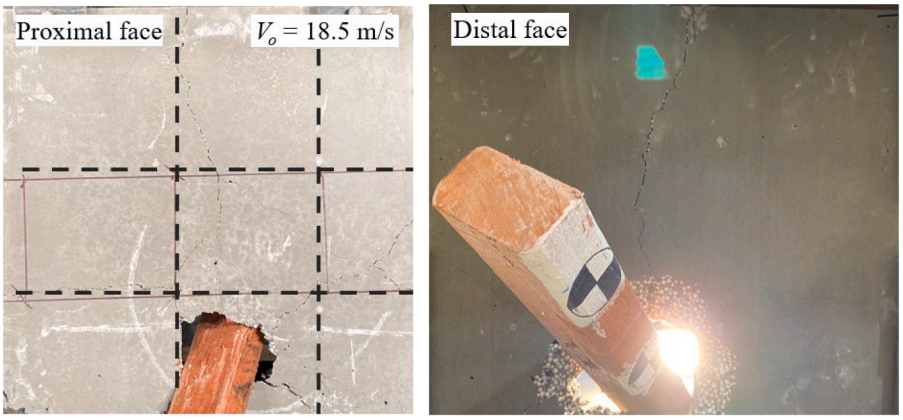

(a) LGC_T37L_PMA

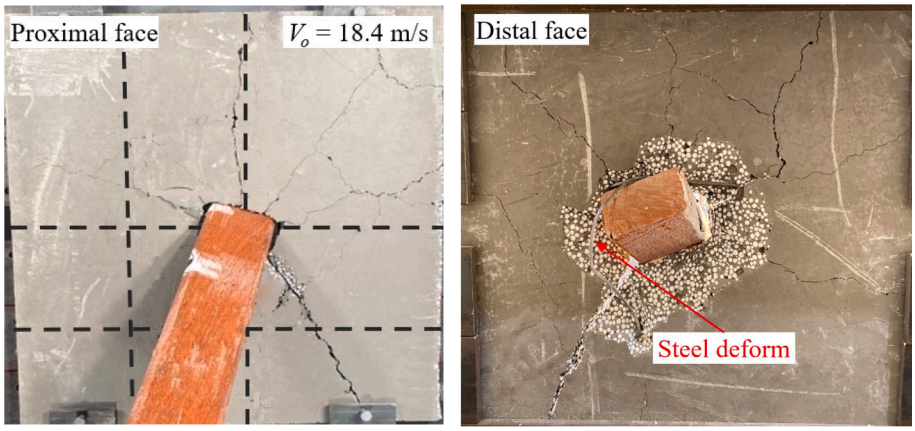

(b) LGC_T37L_WIA

Fig. 15. Photographs of specimens: (a) LGC_T37L_PMA and (b) LGC_T37L_WIA.

the specimen LGC_T50L_SWA. The projectile with the impact velocity of around 23 m/s penetrated through the specimens LGC_T50L_PMB and LGC_T50L_SWB with the rupture of steel mesh. As shown in Fig. 17 (c), if the projectile impacted onto the wire intersection (WI), the specimens failed due to global failure with extensive radial cracks at both proximal and distal faces. The opening was created by scabbing fragments in the impact location at the distal face, and a large piece of LGC was attached to the steel mesh. The specimen failed in flexural–punching mode, indicating that more kinetic energy of the projectile was dissipated. As given in Table 6, for the impact velocity around 18 m/s, the projectile created an opening but was rejected by the wire intersection (LGC_T50L_WIA). The projectile with impact velocities of 24 and 28 m/s resulted in 'penetration and stay' with the penetration length of 129 mm (LGC_T50L_WIB) and 'penetration and through' with the rupture of steel mesh (LGC_T50L_WIC), respectively.

3.2.4. *Failure modes of LGC_T50S*

All LGC_T50S specimens experienced punching–flexural failure. As shown in Fig. 19 (a) and 19(b), the rectangular opening (i.e., 50 mm × 100 mm) and circular opening with radial cracks were observed at the proximal and distal faces, respectively. The projectile impacted onto the steel mesh, causing deformation of steel mesh and cracking in a wider area. When impacting onto steel wire (SW), the projectile with the impact velocity of 18.4 m/s penetrated and stayed in the specimen with the penetration length of 80 mm. The projectile's kinetic energy was partially dissipated by the friction resistance after the penetration and rupture of the steel mesh. The projectile penetrated through the specimens when the impact velocity increased to 23.4 and 28.6 m/s. In addition, it is worth noting that the wire intersection (WI) rejected the projectile under impact velocities of 18.5 and 24.5 m/s. The steel mesh spacing less than the cross-section projectile improved the chance of the projectile striking the steel mesh, indicating that the projectile can be effectively intercepted by the steel mesh with smaller spacing.

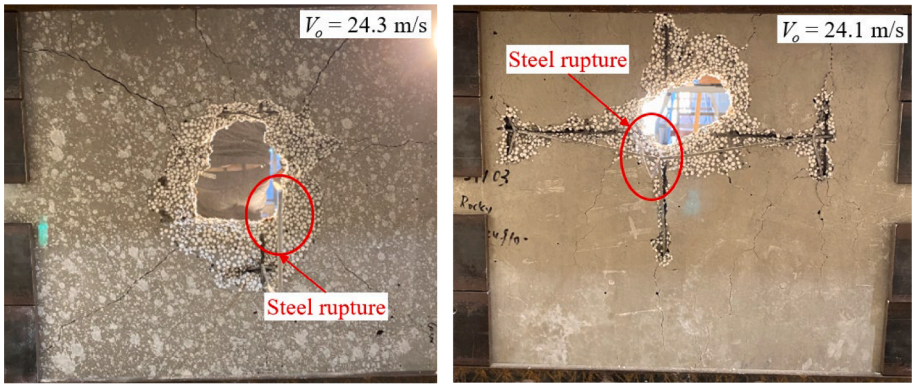

(a) LGC_T37L_SWB (b) LGC_ T37L_WIB

Fig. 16. Photographs of distal face of specimens: (a) LGC_T37L_SWB and (b) LGC_T37L_WIB.

4. Analysis and discussions

In this section, the effects of matrix materials, panel thicknesses, reinforcement spacings and projectile velocities on the impact resistance performance are investigated.

4.1. Effect of matrix material

A comparison on the performance of AAC and LGC panels with the same configurations revealed that the LGC panels have better penetration resistance capacity than AAC panels because LGC has higher strength than AAC and larger inertial resistance to projectile impact because LGC panel is heavier than AAC panel. For example, under the similar impact scenarios, the projectile penetrated and stayed in the specimen LGC_T50L_PMA while penetrated through the specimen AAC_T50L_PMA. The tensile strength of LGC was much higher than that of AAC, which played an essential role in resisting penetration [18,19]. In addition, failure modes of the panels changed due to higher toughness of LGC material, i.e., as shown in Fig. 20, the specimen AAC_T50L_PMA failed in localized punching shear mode with a clear opening at the distal face, but the specimen LGC_T50L_PMA experienced punching–-flexural failure with extensive radial cracks. As observed, the D_{eq} values of LGC specimens were lower than those of AAC specimens in general, which was due to the different mechanical properties of matrix. As given in Table 2, the compressive strength, modulus of rupture and modulus of elasticity of AAC were 4.18 MPa, 0.50 MPa and 1.18 GPa, respectively. LGC exhibited enhancements of 205%, 104%, and 311% in these properties, respectively, indicating higher toughness than AAC material, which leads to the enhanced structural performance. Given the similar input of impact energy, AAC_T50L with inferior mechanical properties of matrix material results in larger D_{eq} than LGC_T50L. Consequently, more kinetic energy can be absorbed by the LGC panel failed in punching–flexural failure with smaller D_{eq} under impact loads due to the superior mechanical properties of matrix material [57–59]. In addition, when the projectile struck the steel mesh, the AAC_T50L specimens experienced more severe damage than the LGC_T50L specimens, which might lead to structural failure due to the decreased stiffness of the whole panel. The opening diameter of the AAC_T50L_WIA specimen was 439 mm at the distal face, which was much larger than that of the LGC_T50L_WIC specimen (312 mm).

It is worth mentioning that the LGC_T37L specimens with the same reinforcement configurations but smaller panel thickness showed better performance in resisting the projectile impacts than AAC_T50L specimens of the same weight under the similar impact scenario. For example, when the impact location was the plain matrix, the projectile with the impact velocity of 18 m/s penetrated through the specimen AAC_T50L_PMA, whereas it penetrated and stayed in the specimen LGC_T37L_PMA with the penetration length of 340 mm. In addition, when the projectile impacted onto the wire intersection, the opening size of LGC_T37L was smaller than that of AAC_T50L; the opening diameter of LGC_T37L specimens ranged from 210 mm to 239 mm, which was much smaller than that of AAC_T50L specimens (i.e., 400 mm). The higher penetration resistance capacity was mainly attributed to the higher LGC material strength, although its thickness was less than that of AAC panels.

4.2. Effect of panel thickness

The LGC_T37L and LGC_T50L specimens had the same reinforcement configurations but different panel thicknesses. As expected, a comparison of the testing results revealed that LGC_T50L had similar failure modes to LGC_T37L but better impact resistance capacity. For instance, when impacting onto the plain matrix at the impact velocity of 18 m/s, the projectile penetrated the specimen LGC_T50L_PMA by 243 mm, and it penetrated the specimen LGC_T37L_PMA by 340 mm. This result was attributed to more kinetic impact energy dissipated by the thicker panel. The panel thickness was found to have a significant effect on the impact resistance capacity and peak impact force in a previous study on RC panels under impact load [60]. The opening size at the distal face D_{eq} had a reverse relation to the thickness of the panels. For example, D_{eq} of LGC_T50L_PMB was 271 mm, whereas that for LGC_T37L_PMB was 206 mm. A similar observation was also reported in a previous study on the impact response of the RC panels [61]. This is because the projectile can perforate a thin panel with less resistance from the panel and cause primarily localized damage, resulting in larger penetration distance or larger residual velocity, while the perforation resistance from a thicker panel is larger, which causes larger global response and spalling damage to the panel. In addition, when impacting on the steel wire at the impact velocity of 18 m/s, the projectile was rejected by LGC_T50L_SWA and LGC_T50L_WIA, whereas it penetrated LGC_T37L_SWA by 340 mm and LGC_T37L_WIA by 295 mm at a similar impact velocity. Thus, with the increased thickness, the perforation resistance capacity increased due to the higher shear and flexural strength of the panel, especially when the projectile impacted onto the steel mesh.

4.3. Effect of reinforcement spacing

To study the effect of steel mesh spacing on the performance of the specimens subjected to windborne debris, the specimens LGC_T50L and LGC_T50S with the same thickness and reinforcement ratio were tested and compared. The projectile rebounded by the specimen LGC_T50S_WIB but penetrated the specimen LGC_T50L_WIB with the penetration length of 129 mm. Additionally, the specimen LGC_T50L_WIB experienced more severe damage than the specimen

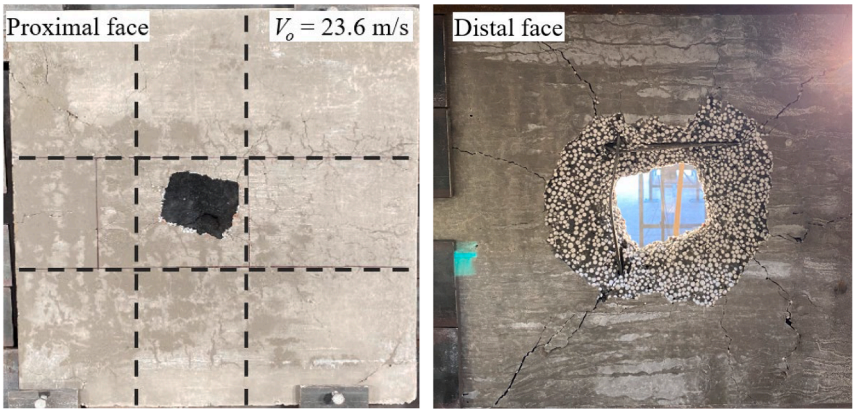

(a) LGC_T50L_PMB

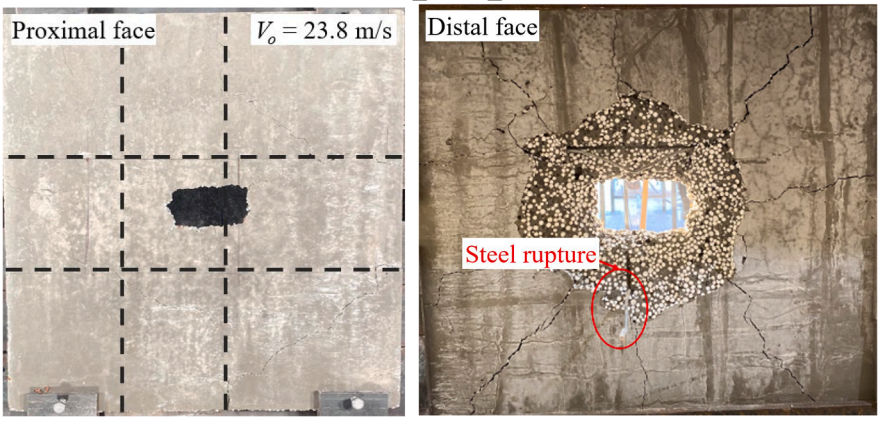

(b) LGC_T50L_SWB

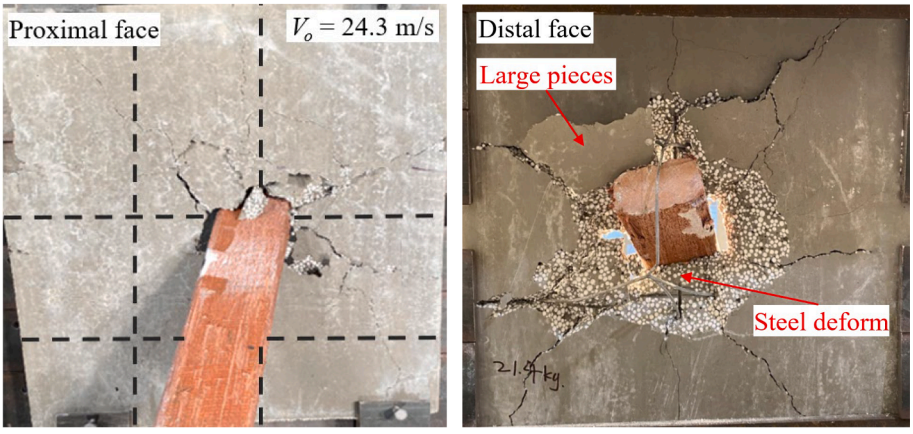

(c) LGC_T50L_WIB

Fig. 17. Photographs of specimens: (a) LGC_T50L_PMB, (b) LGC_T50L_SWB and (c) LGC_T50L_WIB.

Fig. 18. Typical failure process of LGC_T50L at distal face.

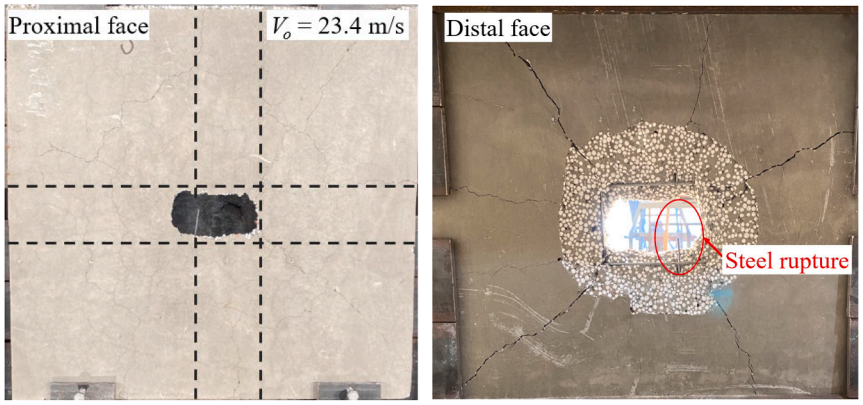

(a) LGC_T50S_SWB

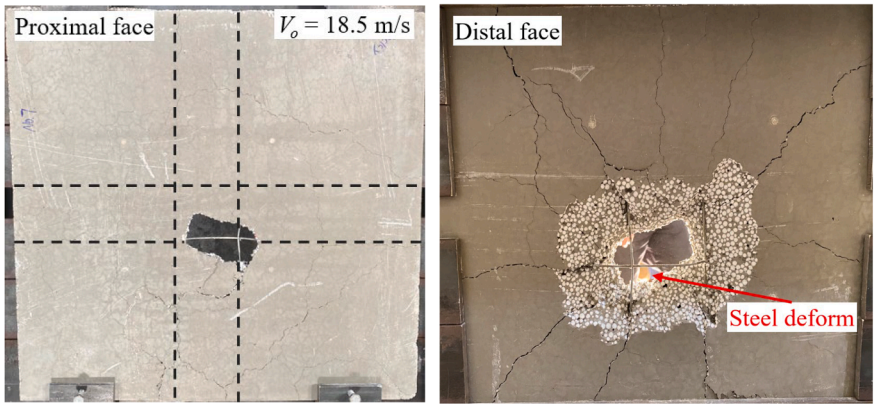

(b) LGC_T50S_WIA

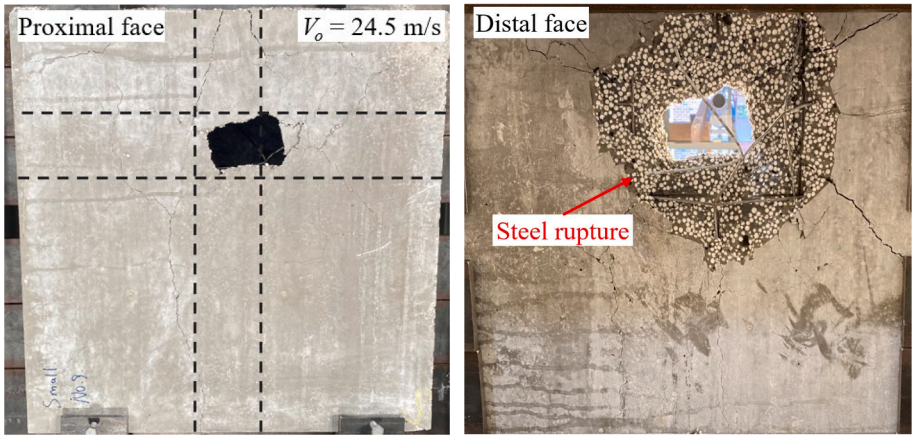

(c) LGC_T50S_WIB

Fig. 19. Photographs of specimens: (a) LGC_T50S_SWB, (b) LGC_T50S_WIA and (c) LGC_T50S_WIB.

LGC_T50S_WIB. LGC_T50L_WIB failed in flexural–punching mode with large pieces attached to the steel mesh, whereas only opening and fewer radial cracks were observed in LGC_T50S_WIB. The opening diameter of LGC_T50S was smaller than that of LGC_T50L in a similar impact scenario. The deformability of the panel was enhanced by using the steel mesh with close spacing [27]; therefore, more impact energy could be dissipated in the form of panel deformation. Thus, denser steel mesh with a constant reinforcement ratio can significantly improve the impact resistance of reinforced lightweight panels.

4.4. *Effect of projectile velocity*

To investigate the performance of the panels under various impact velocities, three projectile velocities (i.e., 18, 23 and 27 m/s) were considered, corresponding to the designed V_R in regions A, B and C defined in AS/NZS 1170.2:2021 [14]. As expected, the specimen subjected to higher impact velocity experienced more severe damage. For the impact velocity of around 18 m/s, the projectile stayed in or rebounded from all the LGC panels with different configurations, whereas only AAC_T50L_WIA survived the projectile impact. For the impact velocity of 23 m/s, the projectile was only rejected by LGC panels when impacting on the wire intersection WI. For the impact velocity of around 27 m/s, the projectile penetrated through all the tested AAC and LGC panels. For the specimen with the thickness of 50 mm, the size of scabbing at the distal face increased with the increase of projectile velocity. For instance, D_{eq} of the specimen LGC_T50L_SWA was 265 mm,

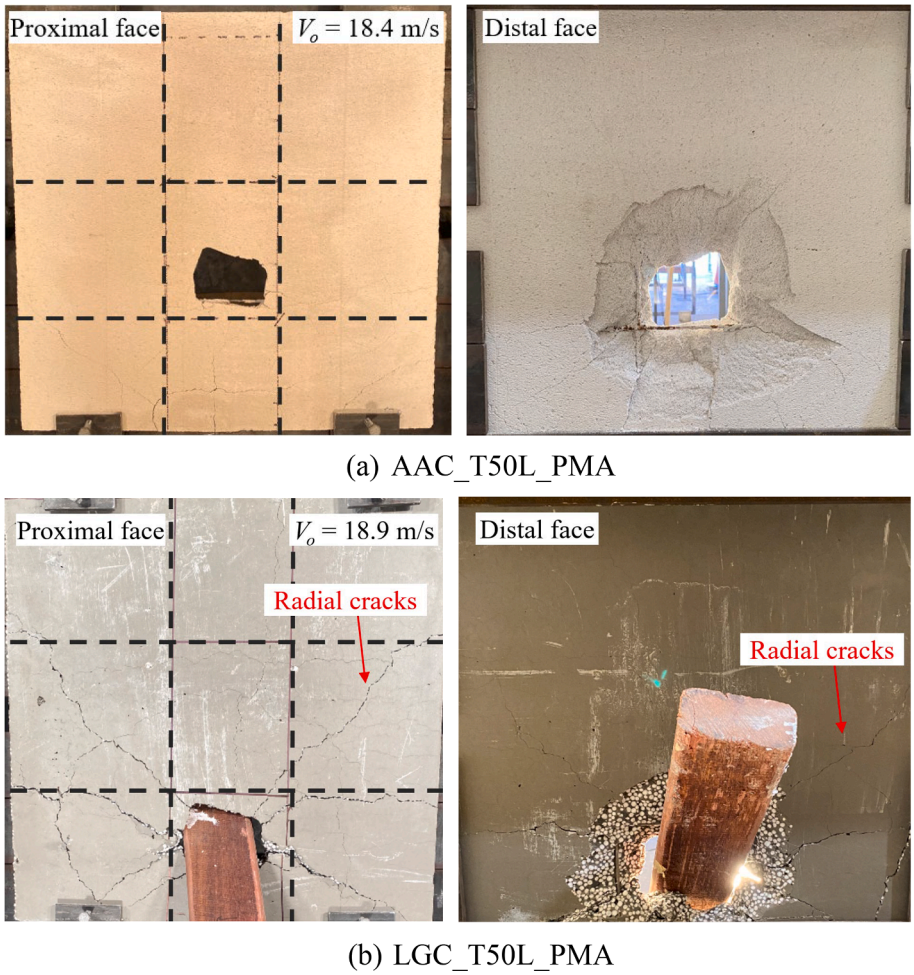

Fig. 20. Photographs of specimens: (a) AAC_T50L_PMA and (b) LGC_T50L_PMA.

and it increased to 297 mm for the specimen LGC_T50L_SWC. For the specimen with the thickness of 37.5 mm, no significant change was observed in the opening size at the distal face; D_{eq} of LGC_T37L_PMA was 202 mm, and it was 206 mm for LGC_T37L_PMB because the projectile perforated these thin panels without causing pronounced global panel response. In addition, with the increase of the impact velocity, the steel mesh experienced damage from large plastic deformation to rupture when the projectile impacted on the wire intersection. For example, LGC_T50L_WIA subjected to impact velocity of 18.8 m/s experienced bending deformation of steel mesh, whereas LGC_T50L_WIC subjected to impact velocity of 28.2 m/s experienced rupture of steel mesh.

5. Conclusion

In this study, AAC panels and LGC panels were investigated under the quasi-static punching shear test and windborne debris impact test. The results showed that LGC panels outperformed the commercially available AAC panels in resisting static and debris impact loads, indicating the potential applications of this panel made of sustainable material in construction. In particular, it was found that:

1) The LGC panels demonstrated better performance than AAC panels because of their higher material strength. Under projectile impact, AAC panels suffered mainly direct perforation failure because of their low shear resistance, while LGC panels suffered mainly combined shear and flexural failure. When the projectile penetrated through the LGC panels, the residual velocities were lower than those after penetrating through the AAC panels because of the higher shear resistance of LGC panels.
2) Using the dense reinforcement mesh in structural panels can significantly enhance their penetration resistance capacity even though the reinforcement ratio is unchanged.
3) None of the tested panels met the design requirement to resist windborne debris impact in strong wind regions as specified in AS/NZS 1170.2:2021, although LGC panels performed better than the AAC panels. For the application of LGC panels in strong wind regions, strengthening measures need to be made to enhance the impact resistance capacity of the panel by increasing the thickness, increasing the reinforcement ratio, attaching FRP sheets on the panel, or a combination of these measures. All these strengthening measures mean increasing the cost and weight, therefore, a systematic study needs be carried out in the future for the applications of LGC panels in strong wind regions.

CRediT authorship contribution statement

Zhixing Li: Conceptualization, Formal analysis, Investigation, Data curation, Writing – original draft. **Wensu Chen:** Conceptualization, Methodology, Supervision, Writing – review & editing. **Hong Hao:** Conceptualization, Funding acquisition, Supervision, Writing – review & editing.

Declaration of Competing Interest

The authors declare that they have no known competing financial

interests or personal relationships that could have appeared to influence the work reported in this paper.

Data availability

Data will be made available on request.

Acknowledgements

The authors acknowledge the financial support from the Australian Research Council (ARC) via Australian Laureate Fellowship (FL180100196).

References

[1] C. Xu, et al., Experimental study on seismic behavior of novel AAC prefabricated panel walls, J. Build. Eng. 44 (2021).
[2] M. D'Orazio, et al., Experimental investigation on the durability of a novel lightweight prefabricated reinforced-EPS based construction system, Constr. Build. Mater. 252 (2020), 119134.
[3] Y. Cui, et al., Failure mechanism of geopolymer composite lightweight sandwich panel under flexural and edgewise compressive loads, Constr. Build. Mater. 270 (2021), 121496.
[4] M.F. Junaid, et al., Lightweight concrete from a perspective of sustainable reuse of waste byproducts, Constr. Build. Mater. 319 (2022), 126061.
[5] Z. Li, et al., Physical and mechanical properties of new lightweight ambient-cured EPS geopolymer composites, J. Mater. Civil Eng. (ASCE) 33 (6) (2021) 04021094.
[6] Z. Li, et al., Dynamic compressive properties of novel lightweight ambient-cured EPS geopolymer composite, Constr. Build. Mater. 273 (2021), 122044.
[7] Z. Li et al., Experimental and analytical study on structural performance of reinforced lightweight geopolymer composites panels, Journal of Building Engineering (Under review).
[8] AS 5146.3: 2018 Reinforced autoclaved aerated concrete-Part 3: Construction, Australian Standard (AS): Committee BD-106, Australia, 2018.
[9] WESTGYP, Nasahi External Walls, https://www.westgyp.com.au/product-category/lightweight-building-materials/. Accessed 17/03 2022.
[10] W. van Boggelen, J. van Boggelen, Sustainable building solutions with new generation autoclaved aerated concrete panel applications, CE/papers 2 (4) (2018) 513–525.
[11] N. Lin, E. Vanmarcke, Windborne debris risk assessment, Probab. Eng. Mech. 23 (4) (2008) 523–530.
[12] J.E. Minor, R.A. Behr, Improving the performance of architectural glazing in hurricanes, Hurricanes of 1992: Lessons learned and implications for the future, ASCE, 1993, pp. 476-485.
[13] S.M. Gebru, Calculation of wind borne debris impact in tornado event, Massachusetts Institute of Technology, 2017.
[14] AS/NZS 1170.2: 2021 Structural design actions-Part 2: Wind actions, Australian/New Zealand Standard (AS/NZS): Joint Technical Committee BD-006, Australia/New Zealand, 2021.
[15] R. Krupar Iii et al., Structural investigation of coastal wind and surge-induced residential building damage caused by Hurricane Harvey 2017.
[16] Fema, Taking shelter from the storm: building a safe room for your home or small business, 3rd ed, Federal Emergency Management Agency, USA, 2008.
[17] Y. Lu, Impact on reinforced concrete structures, Encyclopedia of Continuum Mechanics, Springer2020, pp. 1309-1332.
[18] T. Shirai, et al., Experiment and numerical simulation of double-layered RC plates under impact loadings, Nucl. Eng. Des. 176 (3) (1997) 195–205.
[19] E.F. O'Neil, et al., Tensile properties of very-high-strength concrete for penetration-resistant structures, Shock Vib. 6 (5–6) (1999) 237–245.
[20] A. Dancygier, D. Yankelevsky, High strength concrete response to hard projectile impact, Int. J. Impact Eng 18 (6) (1996) 583–599.
[21] M. Zhang, et al., Resistance of high-strength concrete to projectile impact, Int. J. Impact Eng 31 (7) (2005) 825–841.
[22] M. Abdel-Kader, A. Fouda, Improving the resistance of concrete panels to hard projectile impact, Int. J. Protect. Struct. 10 (4) (2019) 510–538.
[23] X. Chen, et al., Normal perforation of reinforced concrete target by rigid projectile, Int. J. Impact Eng 35 (10) (2008) 1119–1129.
[24] A.N. Dancygier, Effect of reinforcement ratio on the resistance of reinforced concrete to hard projectile impact, Nucl. Eng. Des. 172 (1–2) (1997) 233–245.
[25] M. Abdel-Kader, A. Fouda, Effect of reinforcement on the response of concrete panels to impact of hard projectiles, Int. J. Impact Eng 63 (2014) 1–17.
[26] H. Sadraie, et al., Dynamic performance of concrete slabs reinforced with steel and GFRP bars under impact loading, Eng. Struct. 191 (2019) 62–81.
[27] H. Abbas, et al., Effect of rebar spacing on the behavior of concrete slabs under projectile impact, Struct. Eng. Mech. 77 (3) (2021) 329–342.
[28] N.B. Nevins, Experimental basis for tornado-generated missile impact resistance criteria, Texas Tech University, 1993.
[29] R.R. Carter, Wind-generatd missile impact on composite wall systems, Texas Tech University, 1998.
[30] A. Kulkarni, B. Shafei, Ultra-high performance concrete building wall panels engineered to resist windborne debris impact, J. Build. Eng. 42 (2021), 103004.
[31] W. Chen, H. Hao, Performance of structural insulated panels with rigid skins subjected to windborne debris impacts – Experimental investigations, Constr. Build. Mater. 77 (2015) 241–252.
[32] Q. Meng, et al., Laboratory test and numerical study of structural insulated panel strengthened with glass fibre laminate against windborne debris impact, Constr. Build. Mater. 114 (2016) 434–446.
[33] W. Chen, et al., Failure analysis of corrugated panel subjected to windborne debris impacts, Eng. Fail. Anal. 44 (2014) 229–249.
[34] Q. Meng, et al., Numerical and experimental study of steel wire mesh and basalt fibre mesh strengthened structural insulated panel against projectile impact, Adv. Struct. Eng. 21 (8) (2018) 1183–1196.
[35] Q. Meng, et al., Vulnerability analyses of structural insulated panels with OSB skins strengthened by basalt fiber cloth subjected to windborne debris impact, Int. J. Struct. Stab. Dyn. 18 (06) (2018) 1850088.
[36] Q. Meng, et al., Experimental and numerical study of basalt fibre cloth strengthened structural insulated panel under windborne debris impact, J. Reinf. Plast. Compos. 35 (17) (2016) 1302–1317.
[37] W. Chen, H. Hao, Experimental and numerical study of composite lightweight structural insulated panel with expanded polystyrene core against windborne debris impacts, Mater. Des. 60 (2014) 409–423.
[38] W. Chen, H. Hao, A study of corrolink structural insulated panel (SIP) to windborne debris impacts, Key Engineering Materials, Trans Tech Publ, 2015, pp. 68-73.
[39] NCC 2022, National Construction Code Series, Australian Building Codes Board, Canberra, Australia, 2022.
[40] ASTM, C39-18, Standard test method for compressive strength of cylindrical concrete specimens, West Conshohocken, PA, 2018.
[41] R. Park, W.L. Gamble, Reinforced concrete slabs, John Wiley & Sons, 1999.
[42] M.M. Al-Zahrani, et al., Punching shear capacity of GFRP bar-reinforced concrete slabs-on-ground, Eng. Struct. 289 (2023), 116285.
[43] J.L. Provis, Alkali-activated materials, Cem. Concr. Res. 114 (2018) 40–48.
[44] V. Shobeiri, et al., A comprehensive assessment of the global warming potential of geopolymer concrete, J. Clean. Prod. 297 (2021), 126669.
[45] Z. Jwaida, et al., Geopolymers: The green alternative to traditional materials for engineering applications, Infrastructures 8 (6) (2023) 98.
[46] A. Alsalman, et al., Energy and CO2 emission assessments of alkali-activated concrete and Ordinary Portland Cement concrete: A comparative analysis of different grades of concrete, Clean. Environ. Syst. 3 (2021), 100047.
[47] R. Jones et al., Fly ash route to low embodied CO2 and implications for concrete construction, World of Coal Ash (WOCA) Conference, 2011, pp. 1-14.
[48] The Concrete Centre, The concrete industry sustainability performance 1st report., Camberley, Surrey GU17 9AB., 2009.
[49] G. Hammond, et al., Building services research and information association, University of Bath, Embodied Carbon: The Inventory of Carbon and Energy (ICE), Bath, UK, BSRIA, 2011.
[50] B. Tempest et al., Compressive strength and embodied energy optimization of fly ash based geopolymer concrete, world of coal ash (WOCA) conference, 2009, pp. 1-17.
[51] M. Fawer, et al., Life cycle inventories for the production of sodium silicates, The, Int. J. Life Cycle Assess. 4 (1999) 207–212.
[52] L.K. Turner, F.G. Collins, Carbon dioxide equivalent (CO2-e) emissions: A comparison between geopolymer and OPC cement concrete, Constr. Build. Mater. 43 (2013) 125–130.
[53] S. Prakasan, et al., Study of energy use and CO2 emissions in the manufacturing of clinker and cement, J. Institut. Eng. (India): Series A 101 (2020) 221–232.
[54] A. Talaat, et al., Environmental impact assessment for performance-oriented geopolymer concrete research, J. Mater. Civ. Eng. 35 (1) (2023) 04022370.
[55] T.H. Almusallam, et al., Response of hybrid-fiber reinforced concrete slabs to hard projectile impact, Int. J. Impact Eng 58 (2013) 17–30.
[56] M. Iqbal, The ballistic evaluation of plain, reinforced and reinforced–prestressed concrete, Thin-Walled Struct. 179 (2022), 109707.
[57] R.N. Al-Dala'ien, et al., Failure modes behavior of different strengthening types of RC slabs subjected to low-velocity impact loading: A review, Journal of Composites, Science 7 (6) (2023) 246.
[58] A. Miyamoto, et al., Analysis of failure modes for reinforced concrete slabs under impulsive loads, Structural J. 88 (5) (1991) 538–545.
[59] T.D. Hrynyk, F.J. Vecchio, Behavior of steel fiber-reinforced concrete slabs under impact load, Structural J. 111 (5) (2014) 1213–1224.
[60] N. Kishi et al., Impact resistance of large scale RC slabs, Proceedings of the Second Asia-Pacific Conference on Shock & Impact loads in Structures, Melbourne, Australia, 1997, pp. 213-20.
[61] M. Beppu, et al., Failure characteristics of UHPFRC panels subjected to projectile impact, Compos. B Eng. 182 (2020), 107505.